Acta Materialia 263 (2024) 119533

Contents lists available at ScienceDirect

Acta Materialia

journal homepage: www.elsevier.com/locate/actamat

Full length article

A microstructure-based constitutive model for eutectoid steels

J.R. Páez, A. Dorronsoro, J.M. Martínez-Esnaola, J. Gil Sevillano, J. Alkorta *

CEIT-Basque Research and Technology Alliance (BRTA), Manuel Lardizabal 15, Donostia - San Sebastian, 20018, Spain
Universidad de Navarra, Tecnun, Manuel Lardizabal 13, Donostia - San Sebastian, 20018, Spain

ARTICLE INFO

Keywords:
Constitutive model
Pearlitic steels
Internal stresses
Plasticity
Diffraction

ABSTRACT

This work presents a constitutive model for eutectoid steels based on their two-phase lamellar microstructure. The model accounts for the individual behaviour of both ferrite and cementite, with perfect interphase adhesion assumed. It considers anisotropic hardening mechanisms in ferrite derived from the lamellar structure of pearlite while ignoring the crystal structure of either phase. The model also accounts for the evolution of orientation and spacing of lamellae under directional deformation, along with the evolution of internal stress distribution in both phases. Due to its simplicity, the model has very few calibration parameters but is still able to reproduce complex strain paths and loading conditions with excellent accuracy. The model was compared with tensile, compression and torsion tests from a 13-pass wire drawing series (up to drawing strains of 2.7) and reproduced accurately the mechanical response under any loading condition. The robustness of the model lies in the fact that it is able to recreate the evolution of internal stresses built in cementite and ferrite. Such internal stress evolution was confirmed to reproduce accurately the stress partitioning observed in neutron and X-ray diffraction tests reported in literature. Moreover, the model contributes to the understanding of the rapid broadening of cementite diffraction peaks observed during in-situ tensile tests of patented wires.

1. Introduction

Fully pearlitic eutectoid steels, composed of about 0.8 mass% C plus minor amounts of alloying elements, may offer an excellent compromise of mechanical strength and ductility and are widely employed for rails, pre-stressing tendons and high-strength wires. Pearlite, the product of the eutectoid decomposition of austenite, is a two-phase aggregate of alternating lamellae of 88 vol.% ferrite and 12 vol.% Fe_3C cementite. While ferrite, bcc iron with some elements in solid solution, is ductile above a critical temperature, the bulk orthorhombic iron carbide cementite is hard and brittle. The eutectoid transformation from austenite to pearlite occurs by either slowly cooling down austenite below 727 °C or isothermal treating austenite in the range between the eutectoid temperature and the start of bainite formation, about 550 °C [1–3]. Pearlite is organized in bi-crystalline domains (termed blocks or nodules) constituted of several sub-domains (colonies) whose lamellae share a common spatial orientation. A non-directionally grown as-transformed pearlitic structure, originated from a weakly textured austenite, presents colonies with randomly oriented lamellae and shows mechanical isotropy on the macroscopic length scale. Typically, the as-transformed pearlitic spacing falls in the 50–600 nm range, depending on the transformation temperature (higher undercooling with respect to the equilibrium eutectoid temperature results in smaller spacing). Thus, the thicknesses of pearlitic cementite lamellae are of nanometric size and, embedded in the ferrite lamellae, behave in a ductile manner when pearlite is plastically deformed, particularly in the case of fine pearlites. The size of the colonies is typically an order of magnitude larger than the interlamellar spacing and the influence of the size of both colonies and blocks is of secondary importance for the plastic properties of pearlite with respect to the influence of the interlamellar spacing.

When plastic deformation is applied, e.g., during cold wire drawing, individual colonies stretch along the principal direction of deformation and their pearlitic lamellae reorient accordingly. These progressive lamellar reorientation and stretching are more noticeable if the directional deformation increases to large strains through a monotonic path (e.g., uniaxial deformation, simple shear, even compression, etc.) and are associated to a shrinkage of the average interlamellar spacing. Such refinement of the average pearlitic spacing has a significant strengthening effect.

The experimental values for the yield and flow stress (after a given plastic pre-strain) of fully pearlitic eutectoid carbon steel may be represented by a linear function of either the inverse of the true interlamellar spacing or its square root. Still today, there is much controversy on the

* Corresponding author at: CEIT-Basque Research and Technology Alliance (BRTA), Manuel Lardizabal 15, Donostia - San Sebastian, 20018, Spain.
E-mail addresses: jrpaez@ceit.es (J.R. Páez), adlarbide@ceit.es (A. Dorronsoro), jmesnaola@ceit.es (J.M. Martínez-Esnaola), jgil@ceit.es (J. Gil Sevillano), jalkorta@ceit.es (J. Alkorta).

https://doi.org/10.1016/j.actamat.2023.119533
Received 28 July 2023; Received in revised form 3 November 2023; Accepted 13 November 2023
Available online 15 November 2023

value of the inverse exponent (−1 or −1/2) and the related physical explanation behind each of them [4–9]. Statistical analyses of individual experimental data sets do not provide a clear support for the validity of the −1 or −1/2 exponent. Similarly, statistical analyses integrating several data sets with different chemical composition of the steels, different definitions of the spacings and their measurement methods and different range of the spacings values (e.g., Badeshia and Chintha [9]) lead to conclusions about the preferred strength vs. spacing relationships, in our opinion, questionable.

From a physical point of view, pulling threading dislocations in the ferrite confined between the adjacent assumed impenetrable cementite lamellae (through the dislocation density present in the lamellar ferrite) is necessary for a significant plastic strain. It approximately requires exceeding a critical shear stress, τ_{bow}, for semicircular bowing of the dislocation line on its slip plane limited by the two contiguous cementite plates [10–12],

$$\tau_{bow} = \frac{AGb}{2\pi s_{eff}} \left[\ln\left(\frac{s_{eff}}{b}\right) + B \right] \quad (1)$$

where A is a factor of the order of unity that depends on the character of the dislocation, G = 64 GPa is the shear modulus appropriate for the calculation of the line energy of a $1/2\langle 111\rangle$ screw dislocation in α_{Fe} [13], b = 0.248 nm [14], s_{eff} is the width of ferritic lamellae on its slip plane between its two adjacent cementite plates and B = 0.68 is a parameter related to the energy of the core of the dislocation. Without any fitting parameter, the resolved shear stress given by Eq. (1) multiplied by an orientation factor $M \approx 3$, the Taylor factor commonly used for weakly textured cubic polycrystalline materials, reproduces fairly well the tensile flow stresses of both as-transformed randomly oriented and highly oriented wire drawn pearlite if the strength contribution of cementite to the composite is in both cases accounted for [6]. Moreover, high strength, fine pearlite is a particular case of nanolayered material, and the stress for "confined layer slip", CLS, given by Eq. (1), is currently accepted as a main contribution to the strength of nanolayered metal–metal or metal–ceramic materials [15,16].

After large plastic strains ($\epsilon_{eq} > 2$), signs of cementite dissolution are detected because of the dragging of C atoms from the cementite lamellae by the ferrite dislocations. Volume fraction of cementite lamellae progressively decreases and the carbon content in the ferrite lamellae concurrently increases. At very large strains the lamellar pearlite transforms progressively in a structure of nanometric subgrains/grains with C enriched boundaries which are stabilized and strengthened by C segregation [17–20]. However, in wire drawing, the strengthening progresses at least up to $\epsilon_{eq} = 6.5$, with the strength reaching 7 GPa.

A plethora of multiscale microstructure-based models intended to simulate the stress–strain behaviour of pearlite up to large strains have been published. Refs. [21–34] are only some of them. They span from continuum mechanical models assuming isotropic behaviour of the two constituents of pearlite and simple empirical relationships for the ferrite flow stress vs. its average lamellar spacing evolution to crystal plasticity models of ferrite coupled to FEM (CPFEM) accounting for the evolution of both the spatial orientation of the lamellae and the evolution of the crystallographic orientation of ferrite in each colony, incorporating dislocation density equations and interaction hardening laws for the ferrite slip systems. The crystal plasticity of cementite is not sufficiently known for its incorporation into the models. Finally, it is worth mentioning that several molecular dynamics (MD) simulations of pearlite plastic behaviour have also been made [35–40]. They are invaluable for understanding the nanostructure of pristine ferrite–cementite interface, their function at first deformation stages for interfacial dislocation emission, for characterizing the slip systems in cementite or for showing the effect of ferrite dislocations in the activation of slip dislocations in the cementite. But, of course, current possibilities of MD for pearlite simulations are still limited to very small scale, e.g., to cell calculation sizes of a cementite–ferrite sandwich only several tens of nm thick.

Obviously, if one wants to perform simulations representative of the behaviour of relatively large volumes of pearlitic steel, e.g., to be incorporated in a FEM code for the detailed assessment of multi-pass forming processes like wire drawing or rolling up to large strains, a compromise must be found in the choice of the constitutive model of the material. It must be simple enough to allow for performing a huge amount of computations in a short time, but it cannot be too simple: at least, it must capture the evolution of the microstructure of the lamellar composite, the mechanical evolution of its two phases and of the composite itself and the development of the field of internal stresses at different scales: short range (intra-colony stresses, with distinction of each phase stresses), medium range (single colony-averaged stresses) and long range (macroscopic, stresses averaged in regions of the order of the whole dimensions of the sample, involving many colonies). In this paper, we present a model that offers a good description of microstructural features (and their evolution), combined with the capability of simulating large systems, complex problems up to large deformations with reasonable computational effort. In the model, based on a previous work by Alkorta et al. [41], pearlite is represented as an aggregate of colonies tessellated in elements which, in the unstrained state, share a similar spatial orientation of their lamellae. Each element of pearlite is a ferrite–cementite composite characterized by its interlamellar distance, the spatial orientation of its lamellae and the stress/strain states of its two phases as internal state variables (all of them uniform in the element). Elastic isotropy of both composite phases has been assumed. Ferrite lamellae are considered plastically anisotropic, its plastic constitutive law being mainly controlled by their thickness. Cementite lamellae are treated as elastic perfectly-plastic. The interlamellar spacing and lamellar orientation of each element evolve with applied deformation as in the model developed by Peng et al. [22]. The lamellae are re-oriented with an areal-affine assumption as used by Larijani et al. [28], thus reducing the dense meshing requirement present in CP-FEM approaches. As presented in this paper, the applicability of the model is limited to the range of plastic strains where strain-induced cementite decomposition can be neglected. The ability of the current model to predict the microstructural evolution of eutectoid steels during wire drawing was preliminarily confirmed by Alkorta et al. [41] and will be the subject of a more detailed analysis in a future work.

The paper is structured as follows. First, a detailed description of the mechanical model used for each pearlitic phase is given, pointing out all hardening mechanisms and microstructural properties considered. Then the numerical implementation of the model is described, including the incremental deformation algorithm employed for each phase and the compatibility conditions enforced for the elastoplastic behaviour of the composite. Finally, the accuracy and reliability of the model are tested by performing finite element simulations with a RVE and comparing these results with experimental data.

2. Mesoscopic model of pearlite

2.1. Modelling of pearlitic ferrite

At room temperature or in its neighbourhood and at strain rates roughly in the range of 10^{-4} s^{-1} to 10^{4} s^{-1}, plastic deformation of pearlitic ferrite is carried out by dislocation glide. The long-range glide of dislocation lines (in the sense of large gliding distances relative to effective spacing, s_{eff}) confined on their ferritic slip planes between their two adjacent cementite lamellae requires, in the absence of any local internal stress state, reaching a critical shear stress resolved on their slip plane and in their slip direction, the CRSS. Several sources of resistance to dislocation glide contribute to the CRSS: a friction-like stress, τ_f, strain independent, lumping-up the Peierls stress and the hardening contribution of alien atoms in solid solution; the hardening coming from the strain dependent dislocation density stored in the lamella of ferrite, ρ, approximately proportional to $\sqrt{\rho}$ (Taylor equation), τ_ρ; the also strain dependent overstress required for critically bowing the dislocation line in its situation of confined slip, τ_{bow}, dependent on the

effective interlamellar spacing as per Eq. (1). Assuming additivity for the superposition of these three terms, the CRSS is

$$\tau_{\mathrm{CRSS}} = \tau_{\mathrm{f}} + \tau_{\rho} + \tau_{\mathrm{bow}} \tag{2}$$

A rigorous treatment of the plasticity of pearlitic ferrite demands a crystal plasticity approach with updating, after each strain increment, the crystal orientation, the spatial orientation of the lamellae, the effective spacing of each slip system and the dislocation density of the ferrite of each volume element of pearlite. The overlap of the crystallographic anisotropy with the anisotropy of structural origin significantly modifies the anisotropy of pearlitic ferrite with respect to that of a free ferrite crystal [42]. Simulations of deformation of pearlite considering such overlap have been made (e.g., Watté et al. [21], Van Houtte et al. [43], with the simplifying hypothesis of homogeneous deformation of the colonies of each RVE). However, for performing simulations of multi-pass processes of large size samples up to large strains while keeping good track of the evolution of mechanical properties including internal stresses of short and long range, we are obliged to renounce to a too detailed constitutive model for the sake of computational economy. For instance, instead of explicitly considering the evolution of dislocation densities, for the dislocation hardening term we make use of the Voce hardening equation, which connects with the dislocation density evolution through the Kocks–Mecking relationship [44,45]:

$$\tau_{\rho} = \tau_{\mathrm{sat}} + \left(\tau_0 - \tau_{\mathrm{sat}}\right) \exp\left(-\beta \epsilon_p\right) \tag{3}$$

where τ_0, τ_{sat} and β are material parameters representing the strength at zero plastic strain originated by an initial dislocation density, a saturation strength (corresponding to a saturation of the dislocation density at large strains) and the ratio of the strain hardening rate to $\left(\tau_{\mathrm{sat}} - \tau_0\right)$ at zero plastic strain, respectively. These parameters are calibrated against experimental results. There are alternative models in the literature that provide a better description of strain hardening for a wider range of dislocation densities, such as that of Bouaziz et al. [46,47]. However, in this model we have considered Voce's model for its simplicity.

Furthermore, for our model we have assumed that the essential effect of the fine lamellar structure in the pearlitic plastic anisotropy is to promote shear deformation on the lamellar plane. A "deck of cards" deformation mode (firstly proposed by Langford [5]) is favoured when pearlite colonies are solicited by stress states with a large shear stress component on a soft lamellar plane. The prevalence of the "deck of cards" deformation mode has been many times experimentally observed: e.g., in colonies with lamellar plane tilted near 45° from the stress axis under tensile or compressive axial stresses, or in axially oriented colonies under torsion [48–54]. Therefore, we have adapted the orthotropic plastic yield criterion of Hill [55] to reproduce the "deck of cards" deformation mode in suitably oriented pearlitic elements by assigning adequate values to the parameters of the criterion inspired on the dependence of the CRSS for glide of dislocations on the effective interlamellar spacing, s_{eff}, Eqs. (1) and (2). Fig. 1 shows a pearlitic element with its reference system, where the 3 axis is perpendicular to the lamellae. For the sake of simplicity, we will assume planar isotropy on the lamellar plane (rotational symmetry of the yield criterion around axis 3). Under an applied shear stress τ_{12} we will assume the element will flow in shear, γ_{12}, once the CRSS given by Eq. (2) with $s_{\mathrm{eff}} = s$, is reached (see Fig. 2). It amounts to assume that plastic flow occurs by fictitious dislocations gliding on fictitious slip planes normal to axis 2, with a fictitious Burgers vector parallel to axis 1. Under any shear parallel to the lamellar plane, e.g., τ_{13} or τ_{23}, the lamellar plane is considered a fictitious slip plane for dislocations of fictitious Burgers vector on the slip plane and the glide of dislocations is not constrained by any interlamellar distance. In the absence of any dislocation density in the ferritic lamellae, the glide of such dislocations would only be confined by the boundary of the colony to which the element pertains. Any initial or strain-induced dislocation density will impose a dislocation mean free path, c, and we will consider $s_{\mathrm{eff}} = c$ for calculating the

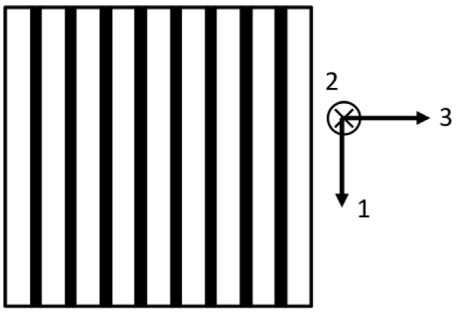

Fig. 1. Reference system of pearlitic colony.

critical bowing stress contribution to the CRSS in this case. According to experimental observations, the dislocation density in the pearlitic lamellae is not homogeneously distributed and the dislocation density is strain dependent. We have considered an explicit dependence of c with the von Mises equivalent strain, ϵ_p through:

$$c\left(\epsilon_p\right) = \frac{K}{\epsilon_p^m} \tag{4}$$

for $\epsilon_p > 0$, where K and m are material constants that are calibrated with the experimental tests. Fig. 3 shows the evolution of c with plastic strain after the calibration procedure. The evolution is aligned with what is observed in literature [56].

As commented above, plastic anisotropy in ferrite has been described using the anisotropic plasticity model proposed by Hill [55] as an extension of the von Mises yield criterion. From now on, we will combine the index convention for stress (and strain) tensors with Voigt's notation, which is very suitable for the description of numerical algorithms. In Voigt's notation, the stress tensor, σ_{ij}, is formulated as a six-component vector that will be denoted as $\boldsymbol{\sigma} = \left[\sigma_{11}, \sigma_{22}, \sigma_{33}, \tau_{12}, \tau_{23}, \tau_{31}\right]^T$. With this convention, the yield locus can be written as

$${}^{\alpha}f = {}^{\alpha}\sigma_{\mathrm{eq}} - {}^{\alpha}\sigma_y = \sqrt{\tfrac{1}{2}\boldsymbol{\sigma}^T \boldsymbol{P}_{\alpha} \boldsymbol{\sigma}} - {}^{\alpha}\sigma_y = 0 \tag{5}$$

The left superscript and subscript α denotes the ferritic phase, σ_y is a certain reference "yield stress" and $\boldsymbol{P}_{\alpha}$ is a tensor that determines the anisotropy of yield. As we have assumed planar isotropy of the criterion on the lamellar plane, normal to axis 3, if we denote $\bar{\sigma}_{ij}$ the yield stresses in the corresponding stress components, then $\bar{\sigma}_{11} = \bar{\sigma}_{22} = \sqrt{3}\bar{\tau}_{12}$ and $\bar{\tau}_{13} = \bar{\tau}_{23}$. Then, $\boldsymbol{P}_{\alpha}$ is expressed as

$$\boldsymbol{P}_{\alpha} = \begin{pmatrix} 2 & N-2 & -N & 0 & 0 & 0 \\ N-2 & 2 & -N & 0 & 0 & 0 \\ -N & -N & 2N & 0 & 0 & 0 \\ 0 & 0 & 0 & 6 & 0 & 0 \\ 0 & 0 & 0 & 0 & 6M & 0 \\ 0 & 0 & 0 & 0 & 0 & 6M \end{pmatrix} \tag{6}$$

where $M = \bar{\tau}_{12}^2/\bar{\tau}_{23}^2 = \bar{\tau}_{12}^2/\bar{\tau}_{13}^2$ and $N = \bar{\sigma}_{11}^2/\bar{\sigma}_{33}^2 = \bar{\sigma}_{22}^2/\bar{\sigma}_{33}^2$. From the previous considerations on the yield under the shear stress components, in combination with the equalities derived from the assumed planar isotropy, we have defined the yield criterion, out of the values of the parameters M and N, which requires the evaluation of the yield stress under the tensile or compressive σ_{33} stress component; we have assumed a fictitious slip plane rotated 45° about the axis 1 or 2 and a fictitious slip direction also inclined 45° with the axis 3 (see Fig. 2(b)), which leads to $\sigma_{33} = 2\tau_{\mathrm{CRSS}}(s_{\mathrm{eff}} = \sqrt{2}s)$, with τ_{CRSS} given by Eq. (2). The strain dependent N and M parameters of the pearlitic elements are updated after each strain increment.

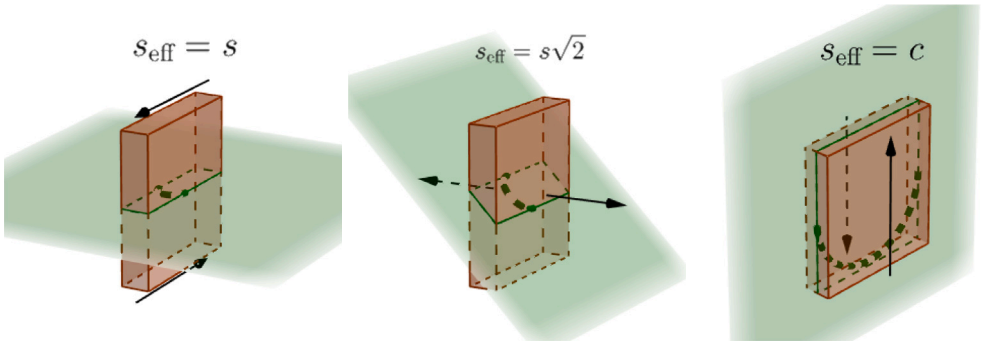

(a) 12 shear (b) 33 tensile (c) 31 shear

Fig. 2. Effective dislocation segments lengths for different glide systems.

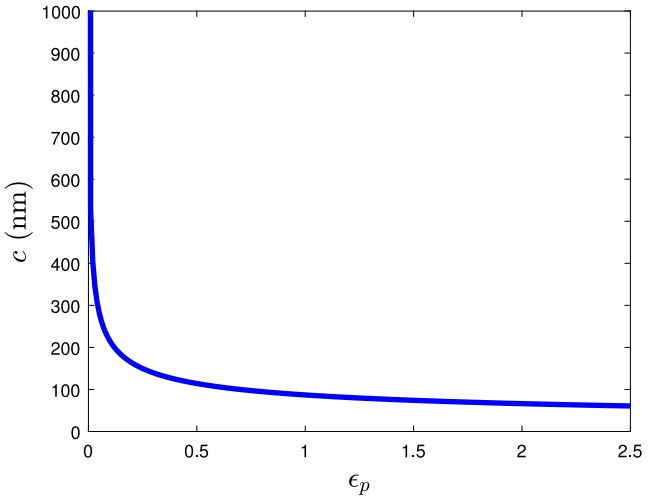

Fig. 3. Evolution of effective dislocation in-plane mean free path, c, as a function of applied equivalent strain.

2.2. Modelling of pearlitic cementite

Cementite is considered mechanically isotropic with elastic perfectly-plastic behaviour. Thus, the counterparts of Eqs. (5) and (6) for cementite are obtained by taking $M = N = 1$, i.e.,

$$ {}^{\theta}f = {}^{\theta}\sigma_{\text{eq}} - {}^{\theta}\sigma_y = \sqrt{\tfrac{1}{2}\boldsymbol{\sigma}^T \boldsymbol{P}_\theta \boldsymbol{\sigma}} - {}^{\theta}\sigma_y = 0 \tag{7} $$

where the left superscript and subscript θ denotes cementite phase and

$$ \boldsymbol{P}_\theta = \begin{pmatrix} 2 & -1 & -1 & 0 & 0 & 0 \\ -1 & 2 & -1 & 0 & 0 & 0 \\ -1 & -1 & 2 & 0 & 0 & 0 \\ 0 & 0 & 0 & 6 & 0 & 0 \\ 0 & 0 & 0 & 0 & 6 & 0 \\ 0 & 0 & 0 & 0 & 0 & 6 \end{pmatrix} \tag{8} $$

With regard to the elastic behaviour, we will consider identical isotropic elastic properties for cementite and ferrite with a Young's modulus of $E = 200$ GPa and a Poisson's ratio of $\nu = 0.3$.

2.3. Ferrite–cementite interface

Perfect adhesion between ferrite and cementite is assumed in this model. Using the reference system depicted in Fig. 1 (note that 3 is the direction normal to the interface), the continuity and equilibrium conditions at the interface can be defined in terms of the Cauchy stress tensor, $\boldsymbol{\sigma}$, and the velocity gradient tensor, $\boldsymbol{L}$, as

$$ {}^{\alpha}\sigma_{13} = {}^{\theta}\sigma_{13};\ {}^{\alpha}\sigma_{23} = {}^{\theta}\sigma_{23};\ {}^{\alpha}\sigma_{33} = {}^{\theta}\sigma_{33} \tag{9} $$

$$ {}^{\alpha}L_{11} = {}^{\theta}L_{11};\ {}^{\alpha}L_{21} = {}^{\theta}L_{21};\ {}^{\alpha}L_{12} = {}^{\theta}L_{12};\ {}^{\alpha}L_{22} = {}^{\theta}L_{22} \tag{10} $$

where α and θ denote, respectively, ferrite and cementite phases.

2.4. Evolution of interlamellar spacing and orientation

Finally, the orientation of the lamellae is defined by their unit normal vector $\boldsymbol{n}$ (2 independent state variables). The evolution of $\boldsymbol{n}$ and the interlamellar spacing, s, with deformation is directly determined by the deformation gradient tensor, $\boldsymbol{F}$, as follows:

$$ \boldsymbol{n} = \frac{\boldsymbol{F}^{-T}\boldsymbol{n}_0}{\left\|\boldsymbol{F}^{-T}\boldsymbol{n}_0\right\|} \tag{11} $$

$$ s = \frac{s_0}{\det(\boldsymbol{F})\left\|\boldsymbol{F}^{-T}\boldsymbol{n}_0\right\|} \tag{12} $$

where $\boldsymbol{n}_0$ is the unit normal vector to the lamella and s_0 is the initial lamellar spacing. Note that $\det(\boldsymbol{F}) = 1$ if the elastic change of volume can be neglected.

3. Numerical implementation of mesoscopic model

3.1. Implicit backward Euler integration algorithm

For the moment we will assume a single-phase elastic–plastic material with the following anisotropic yield locus

$$ f = \sigma_{\text{eq}} - \sigma_y = \sqrt{\tfrac{1}{2}\boldsymbol{\sigma}^T \boldsymbol{P}\boldsymbol{\sigma}} - \sigma_y = 0 \tag{13} $$

Assuming an additive decomposition of the incremental strain in its elastic and plastic components, $\Delta\boldsymbol{\epsilon} = \Delta\boldsymbol{\epsilon}_e + \Delta\boldsymbol{\epsilon}_p$, the corresponding step from the stress $\boldsymbol{\sigma}_o$ at the beginning of the increment to the stress $\boldsymbol{\sigma}_n$ at the end of an increment can be calculated as

$$ \boldsymbol{\sigma}_n = \boldsymbol{\sigma}_o + \boldsymbol{C}\Delta\boldsymbol{\epsilon}_e = \boldsymbol{\sigma}_o + \boldsymbol{C}\left(\Delta\boldsymbol{\epsilon} - \Delta\boldsymbol{\epsilon}_p\right) = \boldsymbol{\sigma}_B - \boldsymbol{C}\Delta\boldsymbol{\epsilon}_p \tag{14} $$

where $\boldsymbol{C}$ is the elastic stiffness tensor and $\boldsymbol{\sigma}_B = \boldsymbol{\sigma}_o + \boldsymbol{C}\Delta\boldsymbol{\epsilon}$ is a trial stress that assumes elastic behaviour during the increment. If $f\left(\boldsymbol{\sigma}_B\right) \le 0$ the material deforms elastically in the incremental step, i.e., $\Delta\boldsymbol{\epsilon}_p = 0$ and $\boldsymbol{\sigma}_n = \boldsymbol{\sigma}_B$. Otherwise, plastic deformation has to be accounted for. The flow rule in Hill's plasticity is defined as:

$$ \Delta\boldsymbol{\epsilon}_p = \Delta\lambda\frac{\partial f}{\partial\boldsymbol{\sigma}} = \frac{\Delta\lambda}{2\sigma_{\text{eq}}}\boldsymbol{P}\boldsymbol{\sigma}_n \tag{15} $$

Then from Eqs. (14) and (15) we obtain

$$ \boldsymbol{\sigma}_n = \left(\boldsymbol{I} + \frac{\Delta\lambda}{2\sigma_{\text{eq}}}\boldsymbol{C}\boldsymbol{P}\right)^{-1}\boldsymbol{\sigma}_B = \boldsymbol{B}^{-1}\boldsymbol{\sigma}_B \tag{16} $$

where $\boldsymbol{I}$ is the 6×6 identity matrix. $\boldsymbol{\sigma}_n$ is solved iterating over Eqs. (13) and (16) using a Newton–Raphson integration scheme. However, this approach is computationally costly since it requires the calculation of the inverse of B, a 6×6 matrix, at every Newton iteration. In this work we circumvent this problem by transforming the stress–strain fields as shown in the following section.

3.1.1. Transformation of stress and strain fields

From now on, we will denote the variables at the transformed space as $\hat{\boldsymbol{x}}$. The proposed transformation stands on the observation that both isotropic elastic stiffness tensor and Hill's anisotropy tensor $\boldsymbol{P}$ (as defined in Eq. (6)) are both diagonalizable and share the same eigenvectors, i.e.:

$$\boldsymbol{C} = \boldsymbol{Q}\hat{\boldsymbol{C}}\boldsymbol{Q}^T \tag{17}$$

$$\boldsymbol{P} = \boldsymbol{Q}\hat{\boldsymbol{P}}\boldsymbol{Q}^T \tag{18}$$

with

$$\boldsymbol{Q} = \begin{pmatrix} \frac{1}{\sqrt{3}} & -\frac{1}{\sqrt{2}} & -\frac{1}{\sqrt{6}} & 0 & 0 & 0 \\ \frac{1}{\sqrt{3}} & \frac{1}{\sqrt{2}} & -\frac{1}{\sqrt{6}} & 0 & 0 & 0 \\ \frac{1}{\sqrt{3}} & 0 & \frac{2}{\sqrt{6}} & 0 & 0 & 0 \\ 0 & 0 & 0 & 1 & 0 & 0 \\ 0 & 0 & 0 & 0 & 1 & 0 \\ 0 & 0 & 0 & 0 & 0 & 1 \end{pmatrix} \tag{19}$$

and $\hat{\boldsymbol{C}}$ and $\hat{\boldsymbol{P}}$ being diagonal matrices with the following diagonal components:

$$\hat{C}_i = \mathrm{diag}\left(\hat{\boldsymbol{C}}\right) = \mathrm{eig}\left(\boldsymbol{C}\right) = [3\lambda + 2\mu,\ 2\mu,\ 2\mu,\ \mu,\ \mu,\ \mu] \tag{20}$$

$$\hat{P}_i = \mathrm{diag}\left(\hat{\boldsymbol{P}}\right) = \mathrm{eig}\left(\boldsymbol{P}\right) = [0,\ 4-N,\ 3N,\ 6,\ 6M,\ 6M] \tag{21}$$

where, λ and μ are Lame's elastic constants (isotropic elasticity). If we consider the following transformation for strains and stresses

$$\hat{\boldsymbol{\sigma}} = \boldsymbol{Q}^T\boldsymbol{\sigma} \tag{22}$$

$$\hat{\boldsymbol{\epsilon}} = \boldsymbol{Q}^T\boldsymbol{\epsilon} \tag{23}$$

then Eqs. (13) and (16) yield

$$f = \sqrt{\tfrac{1}{2}\hat{\boldsymbol{\sigma}}^T\hat{\boldsymbol{P}}\hat{\boldsymbol{\sigma}}} - \sigma_y = \sqrt{\sum_{i=1}^{6}\frac{\hat{P}_i\hat{\sigma}_i^2}{2}} - \sigma_y = 0 \tag{24}$$

and

$$\hat{\boldsymbol{\sigma}}_n = \left(\boldsymbol{I} + \frac{\Delta\lambda}{2\sigma_{\mathrm{eq}}}\hat{\boldsymbol{C}}\hat{\boldsymbol{P}}\right)^{-1}\hat{\boldsymbol{\sigma}}_B = \hat{\boldsymbol{B}}^{-1}\boldsymbol{\sigma}_B \tag{25}$$

with $\hat{\boldsymbol{B}}$ being also a diagonal matrix which can be easily inverted. Finally, combining Eqs. (24) and (25) we get

$$f = \sqrt{\sum_{i=1}^{6}\frac{\hat{P}_i\hat{\sigma}_{Bi}^2}{2\hat{B}_i^2}} - \sigma_y = 0 \tag{26}$$

Note that $\hat{B}_i = \hat{B}_i(\Delta\lambda)$ and $\sigma_y = \sigma_y(\Delta\lambda)$. An iterative Newton–Raphson procedure has been applied to solve Eq. (26).

3.2. Application to pearlitic model

The single-phase elastic–plastic model must be adapted to the two-phase pearlitic model where certain constraints related to the continuity of the ferrite–cementite interface (perfect adhesion criterion, see Section 2.3) must be addressed.

The overall velocity gradient, $\boldsymbol{L}$, is assumed to be the average of the corresponding values in the two phases, i.e., $\boldsymbol{L} = (1-f_{\mathrm{v}})\,{}^{\alpha}\boldsymbol{L} + f_{\mathrm{v}}\,{}^{\theta}\boldsymbol{L}$, where $f_{\mathrm{v}} \sim 0.12$ is the volume fraction of cementite. Then, it is convenient to write the strain increments (in Voigt's notation) in a form that automatically satisfies (10) as

$${}^{\alpha}\Delta\boldsymbol{\epsilon} = \Delta\boldsymbol{\epsilon} + f_{\mathrm{v}}\boldsymbol{\varphi} \tag{27}$$

Table 1
Chemical composition of 0.8wt%C steel.

	C	Mn	Si	Cr	P	S
wt%	0.83	0.53	0.20	0.04	0.011	0.012

$${}^{\theta}\Delta\boldsymbol{\epsilon} = \Delta\boldsymbol{\epsilon} - (1-f_{\mathrm{v}})\,\boldsymbol{\varphi} \tag{28}$$

where $\boldsymbol{\varphi} = \left[0,\ 0,\ \varphi_3,\ 0,\ \varphi_5,\ \varphi_6\right]^T$ is a transfer vector (still to be determined) such that (9) and (10) are fulfilled. In the transformed space we can write

$$\hat{\boldsymbol{\varphi}} = \boldsymbol{Q}^T\boldsymbol{\varphi} = \left[\frac{\varphi_3}{\sqrt{3}},\ 0,\ \frac{2\varphi_3}{\sqrt{3}},\ 0,\ \varphi_5,\ \varphi_6\right]^T \tag{29}$$

The parameters φ_3, φ_5 and φ_6 can be determined analytically by imposing the continuity of tractions at the interface, Eq. (9). The details of the calculations and the final expressions of these parameters are given in Appendix A.

3.3. Integration algorithm for the complete pearlitic model

The constraints represented by vector $\hat{\boldsymbol{\varphi}}$ to guarantee the continuity at the ferrite–cementite interface determine the coupled behaviour of the two phases; this should be accounted for in the numerical procedure to integrate the constitutive equations. Following the integration scheme described in Section 3.1 and recalling Eq. (26), the system of equations to be solved for the coupling of ferrite and cementite phases is now

$${}^{\alpha}f = \sqrt{\sum_{i=1}^{6}\frac{{}^{\alpha}\hat{P}_i\,{}^{\alpha}\hat{\sigma}_{Bi}^2}{2\,{}^{\alpha}\hat{B}_i^2}} - {}^{\alpha}\sigma_y = 0 \tag{30}$$

$${}^{\theta}f = \sqrt{\sum_{i=1}^{6}\frac{{}^{\theta}\hat{P}_i\,{}^{\theta}\hat{\sigma}_{Bi}^2}{2\,{}^{\theta}\hat{B}_i^2}} - {}^{\theta}\sigma_y = 0 \tag{31}$$

Using a Newton–Raphson algorithm to solve the above system, the iteration from step k to $k+1$ can be written as

$$\Delta\boldsymbol{\lambda}^{(k+1)} = \Delta\boldsymbol{\lambda}^{(k)} - \left(\mathbb{J}^{(k)}\right)^{-1}\boldsymbol{f}^{(k)} \tag{32}$$

where

$$\Delta\boldsymbol{\lambda} = \left({}^{\alpha}\Delta\lambda,\ {}^{\theta}\Delta\lambda\right)^T;\ \boldsymbol{f} = \left({}^{\alpha}f,\ {}^{\theta}f\right)^T;\ \mathbb{J} = \begin{pmatrix} \frac{\partial\,{}^{\alpha}f}{\partial\,{}^{\alpha}\Delta\lambda} & \frac{\partial\,{}^{\alpha}f}{\partial\,{}^{\theta}\Delta\lambda} \\ \frac{\partial\,{}^{\theta}f}{\partial\,{}^{\alpha}\Delta\lambda} & \frac{\partial\,{}^{\theta}f}{\partial\,{}^{\theta}\Delta\lambda} \end{pmatrix} \tag{33}$$

Details of the calculation of the Jacobian $\mathbb{J}$ are given in Appendix B. Once the vector of multipliers, $\Delta\boldsymbol{\lambda}$, is calculated, the stress state at the end of the increment for each phase $\omega \in \{\alpha, \theta\}$ is calculated as follows:

$${}^{\omega}\boldsymbol{\sigma}_n = \boldsymbol{Q}\,{}^{\omega}\hat{\boldsymbol{\sigma}}_n = \boldsymbol{Q}\,{}^{\omega}\hat{\boldsymbol{B}}^{-1}\,{}^{\omega}\hat{\boldsymbol{\sigma}}_B \tag{34}$$

where ${}^{\omega}\hat{\boldsymbol{\sigma}}_B$ is given by (A.2). Finally, the overall stress of the colony at the end of the incremental step turns out to be

$$\boldsymbol{\sigma}_n = (1-f_{\mathrm{v}})\,{}^{\alpha}\boldsymbol{\sigma} + f_{\mathrm{v}}\,{}^{\theta}\boldsymbol{\sigma} \tag{35}$$

4. Model calibration

The mesoscopic model for pearlite described in the previous sections is applied here for comparison with the results of tensile, compression and torsion tests performed on 0.8wt%C eutectoid steel wires (see steel composition in Table 1) coming from a 13-pass drawing series supplied by NV Bekaert SA.

Table 2 shows the true nominal strains associated to this series. Each drawn wire was subjected to a set of three tensile tests. In the case of compression tests, small size specimens were cut from passes 0, 6 and 13 with an aspect ratio (length/radius) of about 3, parallel top

Table 2
Description of starting patented 0.8wt%C steel and the series of drawn wires.

Pass	Nominal true strain
0	0.0
1	0.25
2	0.51
3	0.75
4	0.97
5	1.18
6	1.43
7	1.66
8	1.89
9	2.08
10	2.28
11	2.44
12	2.60
13	2.74

and bottom surfaces ($< 1.5°$) carefully prepared with a roughness of $R_a < 0.1$ μm. Torsion tests were also performed on wires from passes 0, 6 and 13.

The experimental results (averaged for 3 specimens) were compared with the results of equivalent virtual tests in a representative volume element (RVE) stretched with periodic boundary conditions [57]. The RVE considered in the finite element computations is shown in Fig. 4. The model consists of a cube of $30 \times 30 \times 30$ elements containing 500 pearlitic colonies, generated using Voronoi tessellation.

In order to simulate the wire drawing process, the RVE was uniaxially stretched using periodic boundary conditions up to strain levels equivalent to those applied in the wire drawing experiments (maximum equivalent strain, $\epsilon_{\text{eq}} = 2.72$, i.e., maximum stretching factor of $l/l_0 \approx 15$). The material properties used in the simulations were calibrated to fit the UTS evolution with drawing strains (see Table 3). Noteworthily, the isotropic hardening associated to Voce-hardening was almost negligible ($\tau_{\text{sat}} - \tau_0 = 20$ MPa) as previously stated by Alkorta et al. [41]. Work hardening in ferrite is, therefore, essentially anisotropic and driven by the reduction of the mean free path for dislocation glide along the in-plane directions (via Eq. (4)). Moreover, although friction stress τ_f in low-alloyed ferrite is typically of the order of some tens of MPa (Peierls stress plus solid solution strengthening), the initial effective dislocation density in patented eutectoid steels can be very large ($\approx 2.6 \cdot 10^{15}$ m^{-2}) as observed by Guelton and François [58], which justifies the large values of $(\tau_f + \tau_0)$ in our calibration (the same authors also show that rate of dislocation storage in pearlitic ferrite at large strains is small, in agreement with our model results of its very weak strain hardening). The best fit value of A was slightly higher than that typically reported in literature ($1 \leq A \leq 1/(1-\nu)$). This deviation could be explained by the effect of crystal anisotropy on the critical shear stress of a Frank–Read source, as observed by [59] or by the effect of the chemical composition on the elastic modulus. In this sense, Cr, Mn and Si, for example, are known to increase the elastic modulus of ferrite [60,61] (see Table 1). With regard to the initial interlamellar spacing of the colonies, we considered that it follows a log-normal distribution with an average size of 120 nm and a standard deviation of 32 nm. These values were obtained from SEM observation on the patented state before drawing. For this purpose, 60 micrographs of the etched surface were taken, and the true interlamellar spacing was calculated using Underwood's method [62].

Fig. 5 shows the comparison between the stress–strain curve resulting from the numerical simulation after an optimal calibration and the UTS experimental data obtained after each of the 13 drawing passes. The model describes very accurately the strain hardening behaviour of the eutectoid steels up to high strain levels. The observed error in UTS is below 2% in all the cases.

Table 3
Calibrated material properties for 0.8wt%C steel.

Parameter	Equation	Value
A	(1)	1.682
$\tau_f + \tau_0$	(2), (3)	300 MPa
$\tau_f + \tau_{\text{sat}}$	(2), (3)	320 MPa
β	(3)	34.48
K	(4)	86.9 nm
m	(4)	0.392
${}^{\theta}\sigma_y$	(7)	4200 MPa

5. Results and discussion

One of the most important advantages of the proposed model is that it is able to account for the evolution of microstructural features such as interlamellar spacing and orientation and also the evolution of internal stresses (stress partitioning) generated by the mismatch in elastic–plastic behaviour of cementite and ferrite phases. In the introductory paper by Alkorta et al. [41], the model showed to be able to reproduce the microstructural evolution of eutectoid steels during wire drawing, highlighting the relevance of anisotropic plasticity of ferritic lamellae on the promotion of the typical curly microstructure in the form of Van Gogh skies [63,64] in the transverse section. Fig. 4(b) shows an example of such distortion calculated with the current model. This enhanced distortion of colonies leads to smaller interlamellar spacings that promote an enhanced strain hardening.

On the other hand, the building of internal stresses during plastic deformation is responsible for the distinct response of drawn wires to different loading conditions, something that has been repeatedly reported elsewhere [65,66]. In the following section, the macroscopic predictions of the model will be compared with experimental strain–stress curves under different loading conditions. The results will also be analysed critically in relation to the reported observations of internal stresses in ferrite and cementite through neutron and X-ray diffraction.

5.1. Mechanical response under tensile, torsion and compression stresses

In order to observe the predictive ability of the model under different loading conditions, three wires corresponding to drawing strains of, respectively, $\epsilon_p = 0.0$, 1.3 and 2.7 were subjected to tensile, torsion and compression tests.

Fig. 6 shows the von Mises equivalent stress–strain response to experimental tensile, torsion and compression tests. The results show that initially (patented wire) the mechanical response is almost identical for all cases. In contrast, the mechanical response for drawn wires becomes increasingly anisotropic with drawing strain. This evolution can be summarized as follows: (1) Drawn wires exhibit an important Bauschinger effect with smaller yield stresses in compression indicative of strong internal back-stresses after drawing. (2) Compression tests show a double kink (specially in passes 0 and 6 and more subtly in pass 13) related to the displaced onset of plasticity of ferrite and cementite phases. For instance, pass 6 shows an initial yield point in compression test at $\approx$ 800 MPa followed by an almost linear hardening up to $\approx$ 1300 MPa where a sudden change in work hardening rate is observed. (3) The strain hardening characteristics are different depending on the strain path: thus, drawn wires (passes 6 and 13) exhibit strain softening in compression and strain hardening in torsion. For comparison, a RVE as that shown in Fig. 4 was subjected to uniaxial straining up to the corresponding nominal drawing strain, unloaded, and then subjected to tensile, compression and simple shear straining. Apart from some minor differences in the initial shape of the curves in tensile and compression tests, the agreement between the experimental tests and the model results is excellent. The slight initial deviations are due to the fact that: (1) The model has simplified the wire drawing procedure by assuming that it is equivalent to uniaxial stretching on a RVE with periodic boundary conditions. This means that the actual deformation

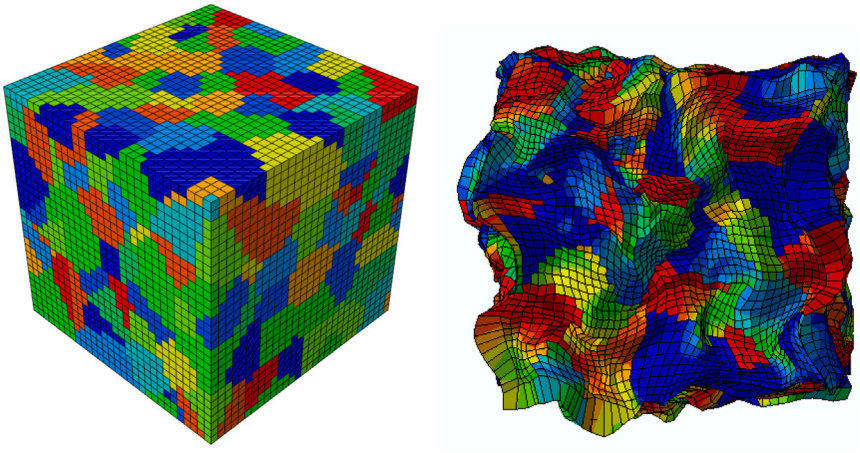

(a) (b)

Fig. 4. (a) Initial 30 × 30 × 30 RVE with ≈ 500 randomly oriented colonies; (b) Cross section mesh distortion after tensile straining with periodic boundary conditions ($\epsilon_p = 2.7$).

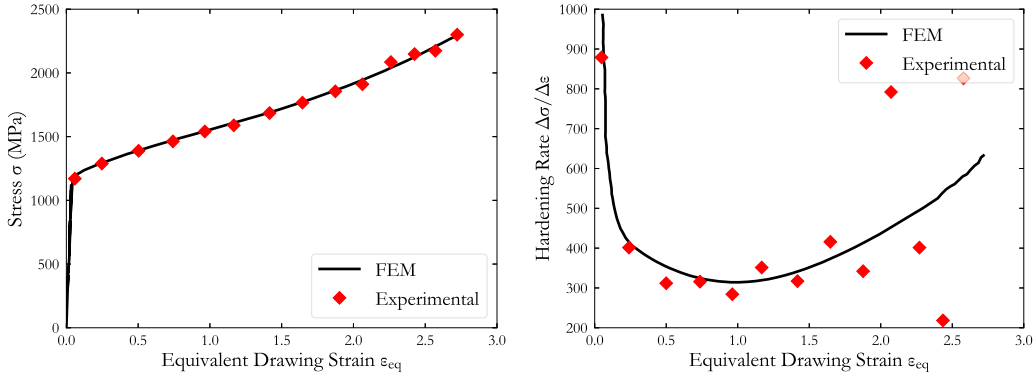

(a) (b)

Fig. 5. (a) Experimental UTS vs. equivalent strain as calculated from the model; (b) work hardening rate derived from the experimental UTS vs. the calculated hardening rates.

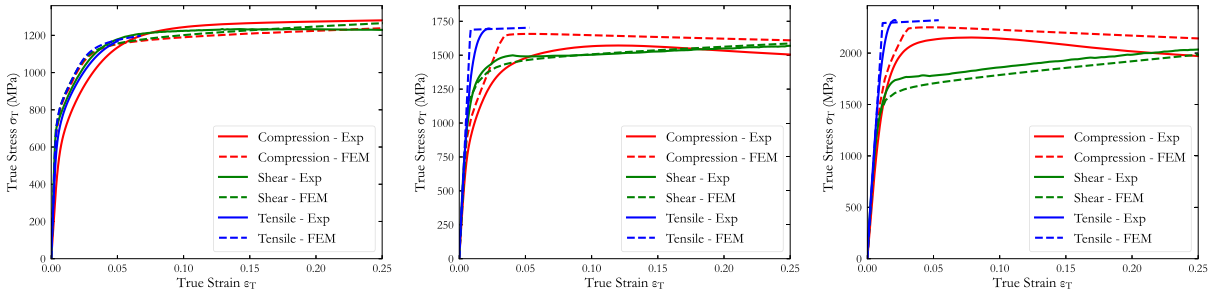

(a) Patented (b) Pass 6 (c) Pass 13

Fig. 6. True stress vs. true strain curves for tensile (blue), torsion (green) and compression tests (red) for drawing passes 0, 6 and 13. The solid and dashed lines correspond, respectively, to the experimental and FEM results. (For interpretation of the references to colour in this figure legend, the reader is referred to the web version of this article.)

history of real wires (which can, moreover, vary from the centre to the surface of the wire) is not accurately considered. (2) Strain rate sensitivity is not included in the model. (3) The compression tests performed with small specimens machined from wires are prone to errors because misalignment and lack of perfect parallelism of the opposed faces of the cylindrical samples. These aspects could explain the smoother behaviour of experimental stress–strain curves for tensile and compression tests.

Despite the simplicity of the considered approach (disregarding the crystalline nature of plasticity of either ferrite or cementite), the model shows its impressive capability of predicting the anisotropic evolution of pearlite for the diverse loading conditions and strain levels considered. First, the Bauschinger effect is precisely detected as can be seen in Fig. 7. Second, the kink due to a delayed onset of plasticity in cementite is captured. Third, the distinct work hardening behaviour of drawn wires under torsion and compression loading is accurately predicted by the model at any drawing strain.

In summary, the results indicate that the model is particularly robust in capturing the different aspects of the evolution of the mechanical response under different levels of drawing strain and under

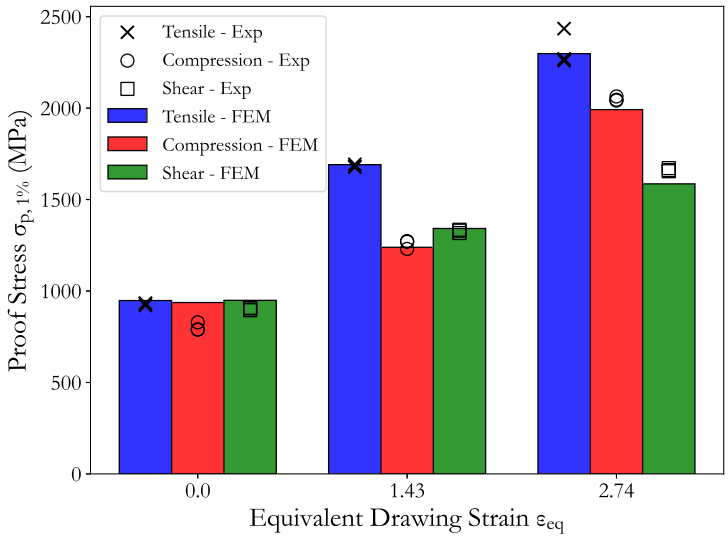

Fig. 7. Experimental results and FEM predictions of 1% proof stress for tensile (blue), torsion (green) and compression tests (red) for drawing passes 0, 6 and 13. (For interpretation of the references to colour in this figure legend, the reader is referred to the web version of this article.)

different loading conditions. This is due, as we will see below, to the fact that the model is able to reproduce the microscopic stress state that is built up during the plastic deformation of eutectoid steels.

5.2. Internal stresses

The evolution of the anisotropic mechanical response after wire drawing is affected by two main aspects of the problem: (1) The microstructural evolution of pearlitic lamellae (orientation and spacing of lamellae); (2) The building of internal stresses during the plastic deformation of pearlite. Both aspects are properly addressed in the proposed model: the former with an evolutionary law described in Eqs. (11) and (12) which has been observed to nicely describe the microstructural evolution of drawn pearlite as observed by Alkorta et al. [41]; the latter is naturally built up as a consequence of the mismatch between the mechanical strength between cementite and ferrite and the perfect interfacial continuity and equilibrium conditions established in Eqs. (9) and (10).

Fig. 8 shows the calculated distribution of internal elastic strains at specific tensile strains (ϵ_{eq} = 0.01, 0.11, 1.43) for cementite and ferrite. Two main conclusions can be derived from these results: first, the average elastic strain in longitudinal direction in cementite is larger than in ferrite confirming the strain partitioning observed in X-ray and neutron diffraction experiments [67–73]; second, the distribution of elastic strains in cementite is, in general, very wide and it develops at relatively low strains. These two different aspects of the results are discussed more deeply below.

5.2.1. Average elastic strains; strain partitioning in pearlite

Fig. 9 shows the evolution of the average internal strains according to the proposed model in both phases during the drawing process (uniaxial stretching). The results confirm that the strain partitioning begins at around 700 MPa (which corresponds to the onset of plasticity in ferrite), reaches a maximum around 1250–1500 MPa and then declines smoothly up to ϵ_{eq} ≈2.7. Note that this decline of the elastic strain partitioning at large drawing strains explains the reduction of Bauschinger effect at pass 13 observed both in experimental and FEM results (see Fig. 7).

Fig. 10(a) shows a compilation of experimental elastic strain measurements compared to the results obtained with the proposed model (thick curves) for patented pearlitic steels. Apart from the experimental data dispersion caused by the wide range of yield strengths and compositions considered (see Table 4 for further details) the model captures the essence of the evolution of elastic strains in both phases and directions. Indeed, the experimental measurements in steels with compositions and yield strengths similar to those of the steel considered in the present work, shows quantitatively very similar results to the calculations made with the model. The model, furthermore, is also able to capture the reversed evolution of elastic strains in ferrite during tensile loading of heavily drawn wires (see Fig. 10(b)). This reversed deviation of elastic strains (compared to the behaviour of patented wires) was first observed by Tomota et al. [71] and justified by a loss of linearity of Hooke's law at elevated elastic stresses. The proposed model shows that, besides anelastic effects, the attenuation of strain partitioning at elevated drawing strains contributes to such deviation. The progressive axial alignment of the lamellae and the lack of strain hardening of cementite are at the origin of such contribution.

In summary, the results demonstrate that the model captures the mechanisms of the development of internal stresses during the plastic deformation of pearlitic steels. This evolution is critical in order to correctly describe the evolution of plastic anisotropy as discussed in Section 5.1.

As pointed out above, the anisotropic evolution of the mechanical response after wire drawing is affected by the evolution of stress partitioning in cementite and ferrite taking place during the plastic deformation of pearlite. Thus, after moderate drawing strains (pass

Table 4
Properties of the fully pearlitic materials corresponding to the internal stresses shown in figure 10; IT: Isothermally transformed; SW+A: Swaged + low temperature annealing; IT+WD: Isothermally Transformed + Wire drawn; AC: Air cooled. See the corresponding references for further information. Yield stress for 0.2% offset strain.

Ref.	Treatment	wt%C	σ_y, MPa
Wang et al. [67]	IT-1	0.82	~ 740
	IT-2	0.82	~ 785
Kanie et al. [68]	SW+A	0.82	1423
Gadalinska et al. [69]	AC-1	0.68	396
	AC-2	0.68	498
Tomota et al. [70]	IT	0.85	930
Tomota et al. [71]	IT+WD	0.88	3800
Shinozaki et al. [72]	IT-1	0.80	507
	IT-2	0.80	659
	IT-3	0.80	808
Adachi et al. [73]	IT	0.80	~ 800
Current work	IT	0.83	689

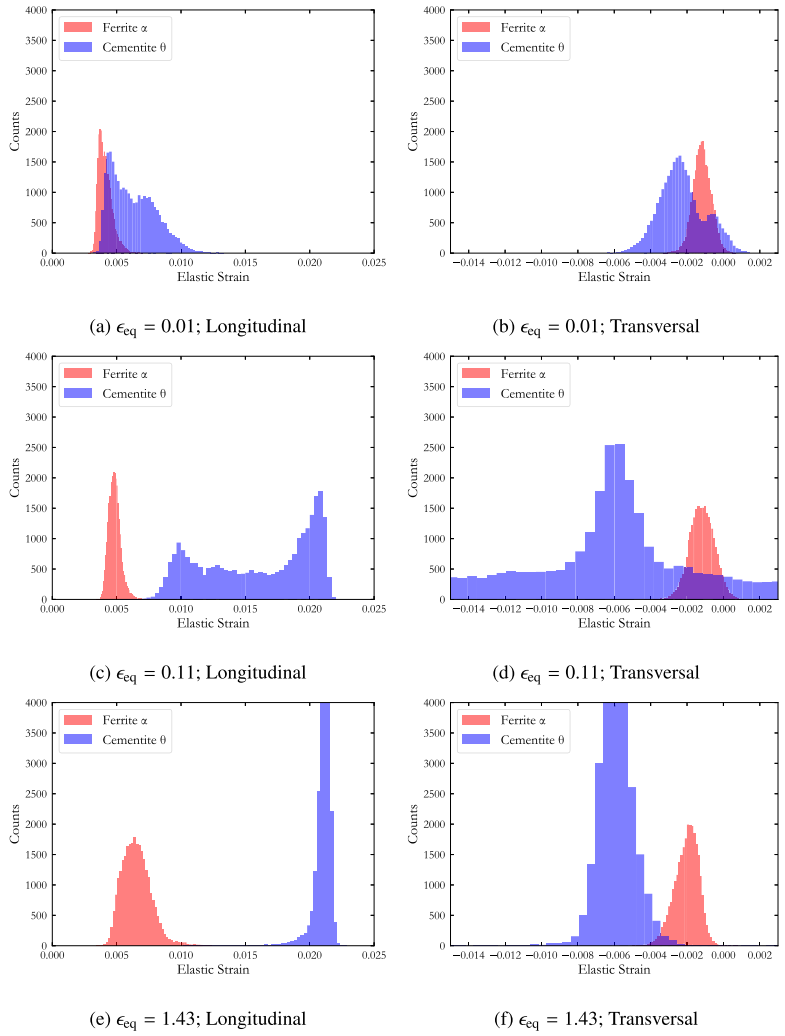

Fig. 8. Internal elastic strain distributions (left: longitudinal; right: transversal) for cementite and ferrite at different drawing strain levels.

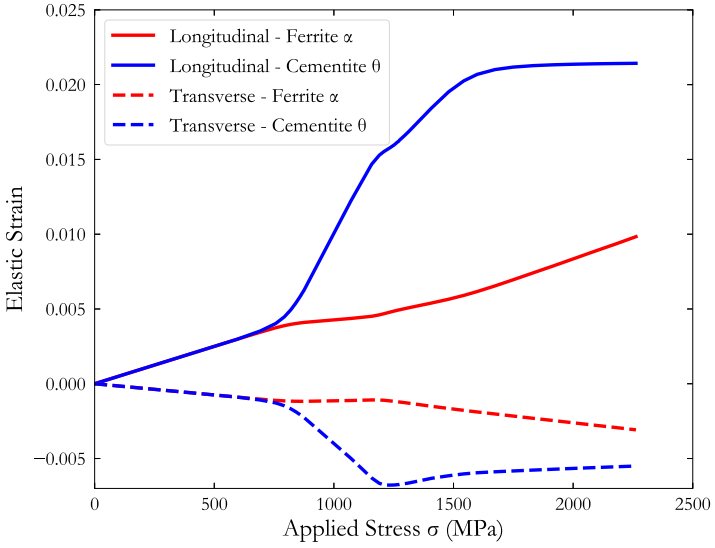

Fig. 9. Evolution of the average elastic strains in cementite (blue lines) and ferrite (red lines) in longitudinal (solid lines) and transverse (dashed lines) directions. (For interpretation of the references to colour in this figure legend, the reader is referred to the web version of this article.)

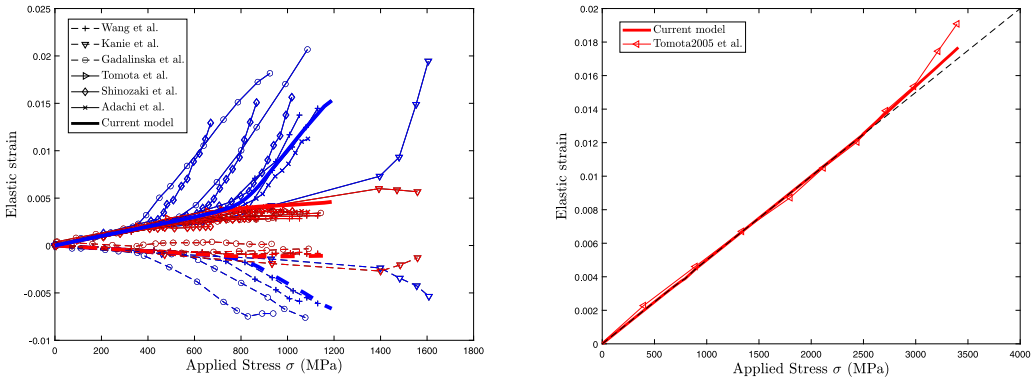

(a) Patented wire

(b) Drawn wire: $\epsilon_{eq} = 4.0$

Fig. 10. Experimental review of the evolution of the average elastic strains in cementite (blue lines) and ferrite (red lines) in longitudinal (solid lines) and transverse (dashed lines) directions for (a) patented and (b) drawn wires. Thick lines correspond to the results of the current model. (For interpretation of the references to colour in this figure legend, the reader is referred to the web version of this article.)

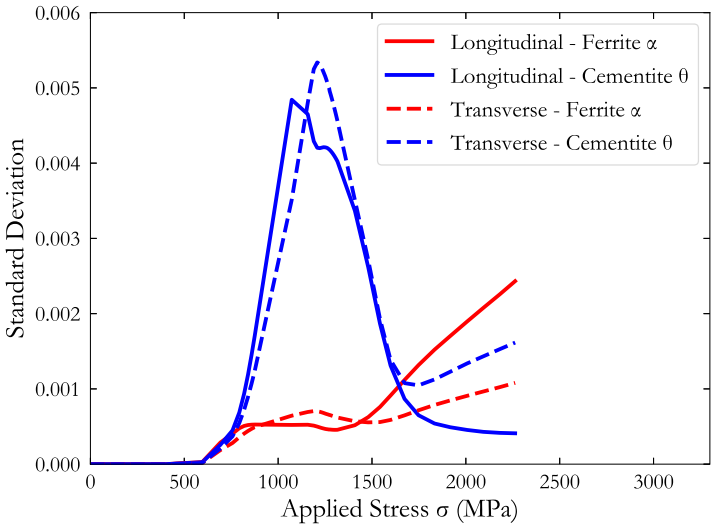

Fig. 11. Standard deviation of internal elastic strain distributions in cementite and ferrite as a function of the applied stress.

6), ferrite develops compressive internal stresses in the longitudinal direction that are compensated with the tensile stresses of cementite. This stress distribution is responsible for an early yield stress (related to the onset of plasticity of ferrite) and a delayed onset of plasticity of cementite (manifested as a kink in the hardening curve at higher stresses). This also explains the reduction of the Bauschinger effect at very high drawing strains (pass 13): as the mechanical strength of ferritic phase increases and the cementite is reaching its plastic strength the mismatch in strength between ferrite and cementite decreases and strain partitioning is mitigated.

5.2.2. Distribution of elastic strains

As discussed above, the results also show that the distribution of elastic strains in cementite widens at relatively low strains, even before the onset of plasticity of cementite (see Fig. 8). This broadening is compatible with the significant peak broadening observed in X-ray and neutron diffraction experiments on in-situ testing of patented pearlitic steels [67,68,74–77]. Fig. 11 shows the standard deviation of the elastic strain distributions of ferrite and cementite as a function of the applied stress calculated with the proposed model. The results show that the distribution of strains in cementite reaches a maximum deviation of 0.005 at an applied stress of $\sigma \approx 1200$ MPa ($\epsilon_{eq} \approx 0.11$) which coincides approximately with the onset of plasticity in cementite; this corresponds to an additional peak broadening of 0.01 times the d-spacing which is in line with the experimental broadening reported in literature [67,74,75].

The accommodation of elastic strains in cementite is highly orientation dependent. As an example, Fig. 12 shows a cross section of the colour map of the longitudinal elastic strain component (ϵ_{33}) of cementite compared to its orientation angle (ϕ). ϕ is the angle between the drawing direction and the normal to the lamellae, i.e., 0° corresponds to lamellae perpendicular to the drawing direction and 90° corresponds to lamellae oriented parallel (with its normal oriented perpendicular) to the drawing direction. The results show a clear correspondence between strain values and orientation. In more detail, Fig. 13 shows the distribution of elastic strains in cementite and ferrite at different applied stresses in longitudinal and transverse directions. Colonies oriented at 45° to drawing direction show minimum elastic strains in cementite in longitudinal direction. This should not be surprising as this is the "softest" loading condition for ferrite (equivalent to 31 shear stress in Fig. 2). Noteworthy, according to Fig. 13, the local elastic strain distribution at a given orientation (width of the distribution for a given ϕ) is similar to that in ferrite; this implies that the origin of the peak broadening in cementite observed in X-ray and neutron diffraction experiments is fully motivated by geometric aspects and the composite nature of pearlite. This confirms the conclusions reached by Weisser et al. [75] on this regard. This is also aligned with the mitigation of the

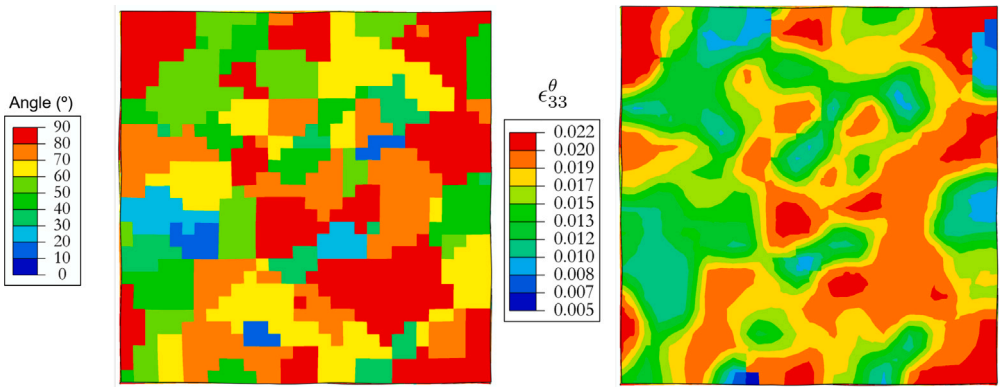

Fig. 12. Colour map representing the colony orientation (top) and its corresponding elastic strain map for cementite in longitudinal direction (bottom) at a total equivalent strain of $\epsilon_{eq} = 0.11$ (applied stress, $\sigma = 1250$ MPa).

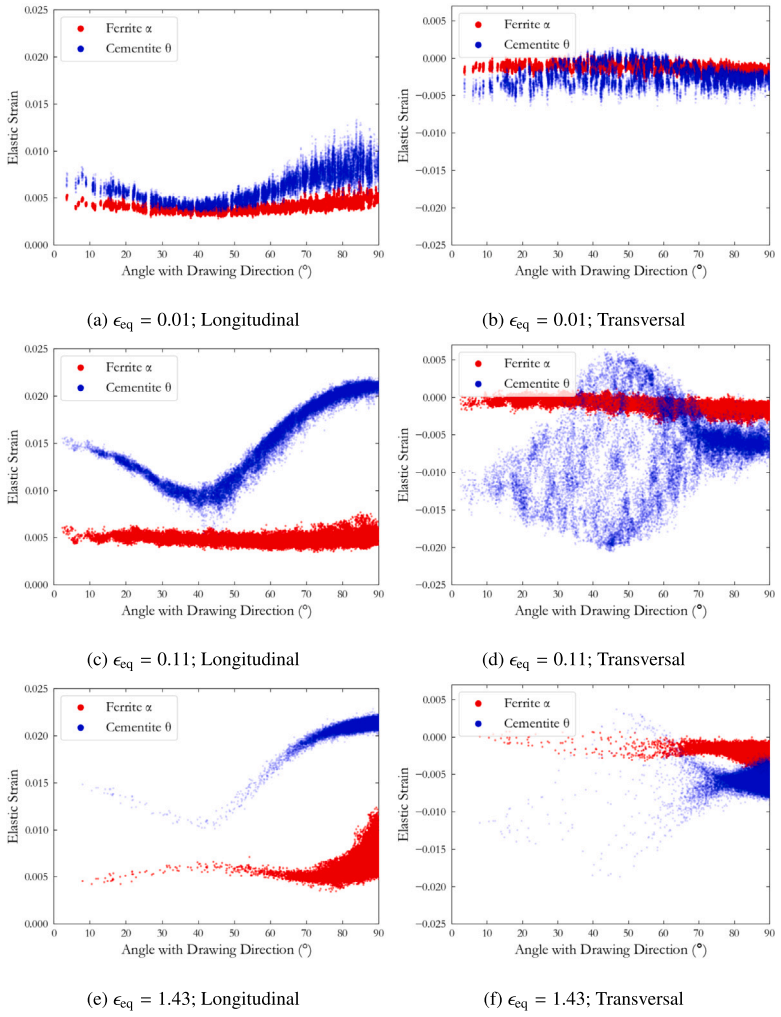

(a) $\epsilon_{eq} = 0.01$; Longitudinal

(b) $\epsilon_{eq} = 0.01$; Transversal

(c) $\epsilon_{eq} = 0.11$; Longitudinal

(d) $\epsilon_{eq} = 0.11$; Transversal

(e) $\epsilon_{eq} = 1.43$; Longitudinal

(f) $\epsilon_{eq} = 1.43$; Transversal

Fig. 13. Internal elastic strain distributions (left: longitudinal; right: transversal) for cementite and ferrite as a function of the lamellar orientation at different drawing strains.

peak broadening observed in chemically extracted cementite through X-ray diffraction with respect to the deformed composite [78,79].

Finally, the strong difference between elastic strain distributions of axial and transverse stresses (Figs. 8 and 13) is easily understandable. The orientation of the lamellae of pearlite deformed by wire drawing is rotationally symmetric around the axial orientation of the wire (for an initial random orientation of the colonies of the undeformed pearlite). Viewed from a transverse direction, such symmetry is lost. The strain state viewed from a random radial direction of the wire depends on the azimuthal angle of the normal to the lamellae. Thus, the strain distribution of ferrite and cementite are broader than the axial counterparts. The broadening of cementite peaks is particularly evident before the lamellae of cementite reach their elastic limit.

6. Conclusions

A novel two-phase anisotropic constitutive model for eutectoid steels has been proposed that efficiently predicts the strain hardening

of eutectoid steels and the anisotropy induced by cold deformation during wire drawing process up to equivalent strains of $\epsilon_{eq} = 2.7$. The model is built using classical descriptions of dislocation glide, considering the effect of dislocation confinement in pearlite but ignoring crystal plasticity. Still, it is able to capture the mechanical response under different loading conditions (in particular, tensile, torsion and compression). The good agreement of the model with the experimental results relies on two main aspects: first, the model is able to reproduce the microstructural evolution in terms of interlamellar spacings and lamellar orientation; and second, the model is able to capture the building up of internal stresses and the evolution of strain partitioning between cementite and ferrite phases. In this regard, the model coincides precisely with the elastic strain measurements done by in-situ X-ray and neutron diffraction and offers a new tool for understanding the plasticity of pearlitic steels beyond the range available in diffraction experiments. For instance, the model clarifies the abnormal broadening of cementite peaks observed in diffraction experiments. Thus, the model shows that a significant contribution to peak broadening at early stages of deformation is not linked to structural defects. Peak broadening can be attributed to the elastic strain dispersion related to the initially randomly oriented lamellar structure of pearlite.

Declaration of competing interest

The authors declare that they have no known competing financial interests or personal relationships that could have appeared to influence the work reported in this paper.

Acknowledgements

The authors would like to thank NV Bekaert SA for funding this research and for their continued support and valuable comments throughout the development of the work.

Appendix A. Calculation of the transfer vector $\hat{\boldsymbol{\varphi}}$

Considering the transformed space, the definition of trial stress and the transfer vector as defined in Eq. (29), the trial stress for each phase can be calculated as:

$$ {}^{\alpha}\hat{\boldsymbol{\sigma}}_B = {}^{\alpha}\hat{\boldsymbol{\sigma}}_o + \hat{\boldsymbol{C}}\left(\Delta\hat{\boldsymbol{\epsilon}} + f_v\hat{\boldsymbol{\varphi}}\right) = {}^{\alpha}\hat{\boldsymbol{s}}_B + f_v\hat{\boldsymbol{C}}\hat{\boldsymbol{\varphi}} \tag{A.1} $$

$$ {}^{\theta}\hat{\boldsymbol{\sigma}}_B = {}^{\theta}\hat{\boldsymbol{\sigma}}_o + \hat{\boldsymbol{C}}\left(\Delta\hat{\boldsymbol{\epsilon}} - \left(1-f_v\right)\hat{\boldsymbol{\varphi}}\right) = {}^{\theta}\hat{\boldsymbol{s}}_B - \left(1-f_v\right)\hat{\boldsymbol{C}}\hat{\boldsymbol{\varphi}} \tag{A.2} $$

where ${}^{\alpha}\hat{\boldsymbol{s}}_B$ and ${}^{\theta}\hat{\boldsymbol{s}}_B$ are, respectively, the apparent trial stresses of ferrite and cementite in the absence of the transfer vector. Then, according to (25) the stress at the end of the increment in each phase can be calculated as follows:

$$ {}^{\omega}\hat{\boldsymbol{\sigma}}_n = {}^{\omega}\hat{\boldsymbol{C}}^{-1}\,{}^{\omega}\hat{\boldsymbol{\sigma}}_B, \text{ for } \omega \in \{\alpha, \theta\} \tag{A.3} $$

Now we impose the continuity of tractions at the interface, Eq. (9),

$$ {}^{\alpha}\sigma^n_{\beta} - {}^{\theta}\sigma^n_{\beta} = \sum_{i=1}^{6} Q_{\beta i}\left[\left(\frac{{}^{\alpha}\hat{s}_i^B}{{}^{\alpha}\hat{B}_i} - \frac{{}^{\theta}\hat{s}_i^B}{{}^{\theta}\hat{B}_i}\right) + Q_{\beta i}\hat{C}_i\hat{\varphi}_j\left(\frac{1-f_v}{{}^{\alpha}\hat{B}_i} + \frac{f_v}{{}^{\theta}\hat{B}_i}\right)\right] \tag{A.4} $$

where σ^n_{β} are the components of vector $\boldsymbol{\sigma}_n$, for $\beta \in \{3, 5, 6\}$, and $\hat{s}_i^B$ are the components of vector $\hat{\boldsymbol{s}}_B$. φ_i can be obtained by solving the system of equations in (A.4).

Appendix B. Calculation of the Jacobian $\mathbb{J}$

The elements of the Jacobian matrix $\mathbb{J}$ in Eq. (33) are calculated as follows:

$$ J_{\omega\psi} = \frac{\partial\,{}^{\omega}f}{\partial\,{}^{\psi}\Delta\lambda} = \frac{\partial\,{}^{\omega}\sigma_{eq}}{\partial\,{}^{\psi}\Delta\lambda} - \frac{\partial\,{}^{\omega}\sigma_{\psi}}{\partial\,{}^{\psi}\Delta\lambda} = S_{\omega\psi} - A_{\omega\psi} \quad \text{with} \quad \omega,\psi \in \{\alpha,\theta\} \tag{B.1} $$

The second term in (B.1) corresponds to the work-hardening of each phase. As cementite is assumed elastic perfectly-plastic in the model, this term can be written in matrix form as

$$ \mathbb{A} = \begin{pmatrix} \frac{\partial\,{}^{\alpha}\sigma_y}{\partial\,{}^{\alpha}\Delta\lambda} & \frac{\partial\,{}^{\alpha}\sigma_y}{\partial\,{}^{\theta}\Delta\lambda} \\ \frac{\partial\,{}^{\theta}\sigma_y}{\partial\,{}^{\alpha}\Delta\lambda} & \frac{\partial\,{}^{\theta}\sigma_y}{\partial\,{}^{\theta}\Delta\lambda} \end{pmatrix} = \begin{pmatrix} A & 0 \\ 0 & 0 \end{pmatrix} \tag{B.2} $$

To calculate the elements in the first term of (B.1), note that for the two-phase pearlite the trial stresses ${}^{\alpha}\hat{\boldsymbol{\sigma}}_B$ and ${}^{\theta}\hat{\boldsymbol{\sigma}}_B$ depend on the coupling parameters $\boldsymbol{\varphi}$, see Eqs. (A.1) and (A.2). After doing the algebra, these terms can be written in matrix form as

$$ \mathbb{S} = \sum_{i=1}^{6}\left(\mathbb{R}_i^D + \mathbb{R}_i^B\right)\mathbb{B}_i \tag{B.3} $$

where

$$ \mathbb{R}_i^D = \begin{pmatrix} \frac{\partial\,{}^{\alpha}\sigma_{eq}}{\partial\,{}^{\alpha}\hat{B}_i} & 0 \\ 0 & \frac{\partial\,{}^{\theta}\sigma_{eq}}{\partial\,{}^{\theta}\hat{B}_i} \end{pmatrix} \tag{B.4} $$

$$ \mathbb{R}_i^B = \sum_{j=1}^{6}\begin{pmatrix} \frac{\partial\,{}^{\alpha}\sigma_{eq}}{\partial\,{}^{\alpha}\hat{\sigma}_j^B}\frac{\partial\,{}^{\alpha}\hat{\sigma}_j^B}{\partial\hat{\varphi}_j}\frac{\partial\hat{\varphi}_j}{\partial\,{}^{\alpha}\hat{B}_i} & \frac{\partial\,{}^{\alpha}\sigma_{eq}}{\partial\,{}^{\alpha}\hat{\sigma}_j^B}\frac{\partial\,{}^{\alpha}\hat{\sigma}_j^B}{\partial\hat{\varphi}_j}\frac{\partial\hat{\varphi}_j}{\partial\,{}^{\theta}\hat{B}_i} \\ \frac{\partial\,{}^{\theta}\sigma_{eq}}{\partial\,{}^{\theta}\hat{\sigma}_j^B}\frac{\partial\,{}^{\theta}\hat{\sigma}_j^B}{\partial\hat{\varphi}_j}\frac{\partial\hat{\varphi}_j}{\partial\,{}^{\alpha}\hat{B}_i} & \frac{\partial\,{}^{\theta}\sigma_{eq}}{\partial\,{}^{\theta}\hat{\sigma}_j^B}\frac{\partial\,{}^{\theta}\hat{\sigma}_j^B}{\partial\hat{\varphi}_j}\frac{\partial\hat{\varphi}_j}{\partial\,{}^{\theta}\hat{B}_i} \end{pmatrix} \tag{B.5} $$

$$ \mathbb{B}_i = \begin{pmatrix} \frac{\partial\,{}^{\alpha}\hat{B}_i}{\partial\,{}^{\alpha}\Delta\lambda} & \frac{\partial\,{}^{\alpha}\hat{B}_i}{\partial\,{}^{\theta}\Delta\lambda} \\ \frac{\partial\,{}^{\theta}\hat{B}_i}{\partial\,{}^{\alpha}\Delta\lambda} & \frac{\partial\,{}^{\theta}\hat{B}_i}{\partial\,{}^{\theta}\Delta\lambda} \end{pmatrix} \tag{B.6} $$

On the other hand, matrix $\boldsymbol{B}_i$ can be written as

$$ \mathbb{B}_i = \mathbb{C}_i\left(\mathbb{I}_2 - \mathbb{D}\cdot\mathbb{S}\right) \tag{B.7} $$

where $\mathbb{I}_2$ is the 2×2 unit matrix,

$$ \mathbb{C}_i = \begin{pmatrix} \frac{\hat{C}_i\,{}^{\alpha}\hat{P}_i}{2\,{}^{\alpha}\sigma_{eq}} & 0 \\ 0 & \frac{\hat{C}_i\,{}^{\theta}\hat{P}_i}{2\,{}^{\theta}\sigma_{eq}} \end{pmatrix} \tag{B.8} $$

and

$$ \mathbb{D} = \begin{pmatrix} \frac{{}^{\alpha}\Delta\lambda}{{}^{\alpha}\sigma_{eq}} & 0 \\ 0 & \frac{{}^{\theta}\Delta\lambda}{{}^{\theta}\sigma_{eq}} \end{pmatrix} \tag{B.9} $$

Substituting (B.7) into (B.3), we can solve for $\mathbb{S}$ to obtain

$$ \mathbb{S} = \left(\mathbb{I}_2 + \mathbb{K}\cdot\mathbb{D}\right)^{-1}\mathbb{K} \tag{B.10} $$

with

$$ \mathbb{K} = \sum_{i=1}^{6}\left(\mathbb{R}_i^D + \mathbb{R}_i^B\right)\mathbb{C}_i \tag{B.11} $$

Finally, the Jacobian $\mathbb{J}$ is calculated from (B.2) and (B.10) as

$$ \mathbb{J} = \mathbb{S} - \mathbb{A} \tag{B.12} $$

References

[1] D. Llewellyn, R. Hudd, Steels: Metallurgy and Applications, Elsevier, 1998.
[2] D.A. Porter, K.E. Easterling, M.Y. Sherif, Phase Transformations in Metals and Alloys, CRC Press, 2021.
[3] H.K. Bhadeshia, Theory of Transformations in Steels, CRC Press, 2021.
[4] T. Gladman, F. Pickering, Some aspects of the structure-property relationships in high-carbon ferrite-pearlite steels, 1972.
[5] G. Langford, Deformation of pearlite, Metall. Trans. A 8 (1977) 861–875.
[6] J. Gil Sevillano, On the yield and flow stress of lamellar pearlite, in: Strength of Metals and Alloys, Elsevier, 1979, pp. 819–824.
[7] D. Alexander, I. Bernstein, Cleavage fracture in pearlitic eutectoid steel, Metall. Trans. A 20 (1989) 2321–2335.
[8] J. Gil Sevillano, A twist on heavily drawn wires, Wire J. Int. 44 (2) (2011) 58–70.
[9] H. Bhadeshia, A. Chintha, Critical assessment 41: The strength of undeformed pearlite, Mater. Sci. Technol. 38 (16) (2022) 1291–1299.

[10] A. Foreman, The bowing of a dislocation segment, Philos. Mag. 15 (137) (1967) 1011–1021.

[11] D.J. Bacon, U.F. Kocks, R.O. Scattergood, The effect of dislocation self-interaction on the orowan stress, Philos. Mag.: J. Theor. Exp. Appl. Phys. 28 (6) (1973) 1241–1263, http://dx.doi.org/10.1080/14786437308227997.

[12] S. Queyreau, G. Monnet, B. Devincre, Orowan strengthening and forest hardening superposition examined by dislocation dynamics simulations, Acta Mater. 58 (17) (2010) 5586–5595, http://dx.doi.org/10.1016/j.actamat.2010.06.028.

[13] J. Hirth, T. Jo/ssang, J. Lothe, Dislocation energies and the concept of line tension, J. Appl. Phys. 37 (1) (1966) 110–116.

[14] H. Frost, M. Ashby, Deformation-Mechanism Maps: the Plasticity and Creep of Metals and Ceramics(Book), Pergamon Press, Oxford, 1982, p. 175, 1982.

[15] A. Misra, J. Hirth, R. Hoagland, Length-scale-dependent deformation mechanisms in incoherent metallic multilayered composites, Acta Mater. 53 (18) (2005) 4817–4824.

[16] I.J. Beyerlein, Z. Li, N.A. Mara, Mechanical properties of metal nanolaminates, Annu. Rev. Mater. Res. 52 (2022) 281–304.

[17] Y. Li, P. Choi, C. Borchers, S. Westerkamp, S. Goto, D. Raabe, R. Kirchheim, Atomic-scale mechanisms of deformation-induced cementite decomposition in pearlite, Acta Mater. 59 (10) (2011) 3965–3977.

[18] Y. Li, D. Raabe, M. Herbig, P.-P. Choi, S. Goto, A. Kostka, H. Yarita, C. Borchers, R. Kirchheim, Segregation stabilizes nanocrystalline bulk steel with near theoretical strength, Phys. Rev. Lett. 113 (10) (2014) 106104.

[19] A. Lamontagne, V. Massardier, X. Kleber, X. Sauvage, D. Mari, Comparative study and quantification of cementite decomposition in heavily drawn pearlitic steel wires, Mater. Sci. Eng. A 644 (2015) 105–113.

[20] N. Guelton, M. François, Strain-induced dissolution of cementite in cold-drawn pearlitic steel wires, Metall. Mater. Trans. A 51 (2020) 1602–1613.

[21] P. Watté, P. Van Houtte, E. Aernoudt, J. Gil Sevillano, W. Van Raemdonck, I. Lefever, H. Bunge, The work hardening of pearlite during wire drawing, in: Materials Science Forum, Vol. 157, no. pt 2, 1994 Trans Tech Publications, Switzerland, 1994.

[22] X. Peng, J. Fan, J. Zeng, Microstructure-based description for the mechanical behavior of single pearlitic colony, Int. J. Solids Struct. 39 (2) (2002) 435–448.

[23] A. Elwazri, P. Wanjara, S. Yue, The effect of microstructural characteristics of pearlite on the mechanical properties of hypereutectoid steel, Mater. Sci. Eng. A 404 (1–2) (2005) 91–98.

[24] X. Hu, P. Van Houtte, M. Liebeherr, A. Walentek, M. Seefeldt, H. Vandekinderen, Modeling work hardening of pearlitic steels by phenomenological and taylor-type micromechanical models, Acta Mater. 54 (4) (2006) 1029–1040.

[25] S. Allain, O. Bouaziz, Microstructure based modeling for the mechanical behavior of ferrite–pearlite steels suitable to capture isotropic and kinematic hardening, Mater. Sci. Eng. A 496 (1–2) (2008) 329–336.

[26] I. Watanabe, D. Setoyama, N. Nagasako, N. Iwata, K. Nakanishi, Multiscale prediction of mechanical behavior of ferrite–pearlite steel with numerical material testing, Internat. J. Numer. Methods Engrg. 89 (7) (2012) 829–845.

[27] E. Lindfeldt, M. Ekh, Multiscale modeling of the mechanical behaviour of pearlitic steel, Technische Mechanik-Eur. J. Eng. Mech. 32 (2–5) (2012) 380–392.

[28] N. Larijani, G. Johansson, M. Ekh, Hybrid micro–macromechanical modeling of anisotropy evolution in pearlitic steel, Eur. J. Mech. A Solids 38 (2013) 38–47.

[29] N. Larijani, C. Kammerhofer, M. Ekh, Simulation of high pressure torsion tests of pearlitic steel, J. Mater Process. Technol. 223 (2015) 337–343.

[30] Y. Yasuda, T. Ohashi, Crystal plasticity analyses of scale dependent mechanical properties of ferrite/cementite lamellar structure model in pearlite steel wire with Bagaryatsky or Pitsch-Petch orientation relationship, ISIJ Int. 56 (12) (2016) 2320–2326.

[31] M. Ekh, N. Larijani, E. Dartfeldt, M. Kapp, R. Pippan, Prediction of the mechanical behaviour of pearlitic steel based on microcompression tests, micromechanical models and homogenization approaches, Eur. J. Mech. A Solids 67 (2018) 272–279.

[32] S. Isavand, A. Assempour, Strain localization and deformation behavior in ferrite-pearlite steel unraveled by high-resolution in-situ testing integrated with crystal plasticity simulations, Int. J. Mech. Sci. 200 (2021) 106441.

[33] S. Isavand, M. Kardan-Halvaei, A. Assempour, Crystal plasticity modeling and experimental characterization of strain localization and forming limits in ferrite-pearlite steels, Int. J. Solids Struct. 233 (2021) 111205.

[34] X. Huang, J. Wang, S. Zhao, Z. Yao, C. Liu, High-resolution multiscale modeling of mechanical behavior of cold-drawn pearlitic steels, J. Mater. Res. Technol. 15 (2021) 5920–5935.

[35] J. Kim, H. Ghaffarian, S. Ryu, K. Kang, The effect of the misfit dislocation on the in-plane shear response of the ferrite/cementite interface, Comput. Mater. Sci. 173 (2020) 109375.

[36] J. Kim, H. Ghaffarian, K. Kang, The lattice dislocation trapping mechanism at the ferrite/cementite interface in the Isaichev orientation relationship, Sci. Rep. 11 (1) (2021) 1–8.

[37] T. Shimokawa, T. Niiyama, M. Okabe, J. Sawakoshi, Interfacial-dislocation-controlled deformation and fracture in nanolayered composites: Toward higher ductility of drawn pearlite, Acta Mater. 164 (2019) 602–617.

[38] M. Guziewski, S.P. Coleman, C.R. Weinberger, Interface energetics and structure of the pearlitic microstructure in steels: An atomistic and continuum investigation, Acta Mater. 155 (2018) 1–11.

[39] M. Guziewski, S.P. Coleman, C.R. Weinberger, Atomistic investigation into interfacial effects on the plastic response and deformation mechanisms of the pearlitic microstructure, Acta Mater. 180 (2019) 287–300.

[40] L.-W. Liang, Y.-J. Wang, Y. Chen, H.-Y. Wang, L.-H. Dai, Dislocation nucleation and evolution at the ferrite-cementite interface under cyclic loadings, Acta Mater. 186 (2020) 267–277.

[41] J. Alkorta, J. Martínez-Esnaola, P. de Jaeger, J.G. Sevillano, New mesoscopic constitutive model for deformation of pearlitic steels up to moderate strains, IOP Conf. Ser.: Mater. Sci. Eng. 219 (1) (2017) 012010, http://dx.doi.org/10.1088/1757-899X/219/1/012010.

[42] J.G. Sevillano, P. Van Houtte, E. Aernoudt, Plastic anisotropy of pearlitic ferrite, Textures Mater. 2 (1978) 495–504.

[43] P. Van Houtte, P. Watté, E. Aernoudt, J. Gil Sevillano, I. Lefever, W. Van Raemdonck, Taylor simulation of cyclic textures at the surface of drawn wires using a simple flow field model, in: Materials Science Forum, Vol. 157, Trans Tech Publ, 1994, pp. 1881–1886.

[44] H. Mecking, U. Kocks, Kinetics of flow and strain-hardening, Acta Metall. 29 (11) (1981) 1865–1875.

[45] U. Kocks, H. Mecking, Physics and phenomenology of strain hardening: The FCC case, Prog. Mater. Sci. 48 (3) (2003) 171–273.

[46] O. Bouaziz, Revisited storage and dynamic recovery of dislocation density evolution law: Toward a generalized kocks–mecking model of strain-hardening, Adv. Eng. Mater. 14 (9) (2012) 759–761.

[47] O. Bouaziz, D. Lloyd, Assessment of a physical based modelling suitable to capture the mechanical behaviour at large plastic strain of aluminium alloys, Metall. Res. Technol. 119 (4) (2022) 419.

[48] Y. Liu, A. Tidu, B. Bolle, L. Zuo, J.-J. Heizmann, Torsional modelisation of the torsion texture of steel cord, in: Materials Science Forum, Vol. 408, Trans Tech Publications Ltd., Zurich-Uetikon, Switzerland, 2002, pp. 457–462.

[49] Y. Liu, Y. Zhang, A. Tidu, L. Zuo, ⟨110⟩ Fiber texture evolution of ferrite wires during drawn-torsion and drawn-annealing-torsion process, J. Mater. Sci. Technol. 28 (11) (2012) 1010–1014.

[50] M. Kapp, A. Hohenwarter, S. Wurster, B. Yang, R. Pippan, Anisotropic deformation characteristics of an ultrafine-and nanolamellar pearlitic steel, Acta Mater. 106 (2016) 239–248.

[51] A. Hohenwarter, M. Kapp, B. Völker, O. Renk, R. Pippan, Strength and ductility of heavily deformed pearlitic microstructures, IOP Conf. Ser.: Mater. Sci. Eng. 219 (1) (2017) 012003.

[52] A. Jamoneau, D. Solas, J. Bourgon, P. Morisot, J.-H. Schmitt, Strain localization and delamination mechanism of cold-drawn pearlitic steel wires during torsion, Mater. Sci. Eng. A 814 (2021) 141222.

[53] M. Tanaka, Y. Yoshimi, K. Higashida, T. Shimokawa, T. Ohashi, A multiscale approach for the deformation mechanism in pearlite microstructure: Experimental measurements of strain distribution using a novel technique of precision markers, Mater. Sci. Eng. A 590 (2014) 37–43.

[54] T. Teshima, M. Kosaka, K. Ushioda, N. Koga, N. Nakada, Local cementite cracking induced by heterogeneous plastic deformation in lamellar pearlite, Mater. Sci. Eng. A 679 (2017) 223–229.

[55] R. Hill, A theory of the yielding and plastic flow of anisotropic metals, Proc. R. Soc. Lond. Ser. A 193 (1033) (1948) 281–297.

[56] Y. Li, A. Kostka, P. Choi, S. Goto, D. Ponge, R. Kirchheim, D. Raabe, Mechanisms of subgrain coarsening and its effect on the mechanical properties of carbon-supersaturated nanocrystalline hypereutectoid steel, Acta Mater. 84 (2015) 110–123, http://dx.doi.org/10.1016/j.actamat.2014.10.027.

[57] W. Wu, J. Owino, A. Al-Ostaz, L. Cai, Applying periodic boundary conditions in finite element analysis, in: SIMULIA Community Conference, Providence, 2014, pp. 707–719.

[58] N. Guelton, M. François, Microstructure–property relationship in cold-drawn pearlitic steel wires, Metall. Mater. Trans. A 51 (4) (2020) 1543–1566.

[59] I. Kovács, The critical shear stress needed for the operation of a dislocation segment as a frank-read source in anisotropic crystals, Physica Status Solidi (B) 3 (1) (1963) 140–144, http://dx.doi.org/10.1002/pssb.19630030115, arXiv:https://onlinelibrary.wiley.com/doi/pdf/10.1002/pssb.19630030115.

[60] U. Bohnenkamp, R. Sandström, Evaluation of the elastic modulus of steels, Steel Res. 71 (3) (2000) 94–99.

[61] S. Münstermann, Y. Feng, W. Bleck, Influencing parameters on elastic modulus of steels, Can. Metall. Q. 53 (3) (2014) 264–273.

[62] E.E. Underwood, Quantitative stereology for microstructural analysis, in: Microstructural Analysis: Tools and Techniques, Springer, 1973, pp. 35–66.

[63] J. Gil Sevillano, L. Matey Muñoz, J. Flaquer Fuster, Ciels de Van Gogh et propriétés mécaniques, J. Phys. IV 8 (PR4) (1998) Pr4–155.

[64] J. Toribio, Structural integrity of progressively cold-drawn pearlitic steels: From Raffaello Sanzio to Vincent van Gogh, Procedia Struct. Integr. 3 (2017) 3–10.

[65] A. Durgaprasad, S. Giri, S. Lenka, S. Kundu, S. Mishra, S. Chandra, R. Doherty, I. Samajdar, Microstructures and mechanical properties of as-drawn and laboratory annealed pearlitic steel wires, Metall. Mater. Trans. A 48 (2017) 4583–4597.

[66] L. Zhou, F. Fang, M. Kumagai, E. Pickering, X. Zhang, A modified pearlite microstructure to overcome the strength-plasticity trade-off of heavily drawn pearlitic wire, Scr. Mater. 206 (2022) 114236.

[67] Y. Wang, T. Ohnuki, Y. Tomota, S. Harjo, T. Ohmura, Multi-scaled heterogeneous deformation behavior of pearlite steel studied by in situ neutron diffraction, Scr. Mater. 140 (2017) 45–49.
[68] A. Kanie, Y. Tomota, S. Torii, T. Kamiyama, Elastic strains of cementite in a pearlite steel during tensile deformation measured by neutron diffraction, ISIJ Int. 44 (11) (2004) 1952–1956.
[69] E. Gadalińska, A. Baczmański, C. Braham, G. Gonzalez, H. Sidhom, S. Wroński, T. Buslaps, K. Wierzbanowski, Stress localisation in lamellar cementite and ferrite during elastoplastic deformation of pearlitic steel studied using diffraction and modelling, Int. J. Plast. 127 (2020) 102651, http://dx.doi.org/10.1016/j.ijplas.2019.102651.
[70] Y. Tomota, P. Lukáš, D. Neov, S. Harjo, Y. Abe, In situ neutron diffraction during tensile deformation of a ferrite-cementite steel, Acta Mater. 51 (3) (2003) 805–817, http://dx.doi.org/10.1016/S1359-6454(02)00472-X.
[71] Y. Tomota, T. Suzuki, A. Kanie, Y. Shiota, M. Uno, A. Moriai, N. Minakawa, Y. Morii, In situ neutron diffraction of heavily drawn steel wires with ultra-high strength under tensile loading, Acta Mater. 53 (2) (2005) 463–467, http://dx.doi.org/10.1016/j.actamat.2004.10.003.
[72] T. Shinozaki, S. Morooka, T. Suzuki, Y. Tomota, T. Kamiyama, Influence of lamellar spacing on deformation behavior of pearlite steels studied by in situ neutron diffraction, in: The 3rd International Conference on Advanced Structural Steels Gyeongju. Korea, 2006.
[73] Y. Adachi, M. Ojima, S. Morooka, Y. Tomota, Hierarchical 3D/4D characterization on deformation behavior of austenitic and pearlitic steels, in: Materials Science Forum, Vol. 638, Trans Tech Publ, 2010, pp. 2505–2510.
[74] J. Tacq, M. Kriška, M. Seefeldt, Synchrotron diffraction study of the cementite phase in cold drawn pearlitic steel wires, in: Materials Science Forum, Vol. 768, Trans Tech Publ, 2014, pp. 380–387.
[75] M. Weisser, S. Van Petegem, A. Cervellino, H. Van Swygenhoven, On the origin of cementite diffraction peak broadening during tensile deformation at ambient temperatures, Int. J. Plast. 66 (2015) 138–144.
[76] K. Van Acker, J. Root, P. Van Houtte, E. Aernoudt, Neutron diffraction measurement of the residual stress in the cementite and ferrite phases of cold-drawn steel wires, Acta Mater. 44 (10) (1996) 4039–4049.
[77] K. Inal, J. Lebrun, M. Belassel, Second-order stresses and strains in heterogeneous steels: Self-consistent modeling and X-ray diffraction analysis, Metall. Mater. Trans. A 35 (2004) 2361–2369.
[78] S. Sato, K. Wagatsuma, M. Ishikuro, E.-P. Kwon, H. Tashiro, S. Suzuki, Precise characterization of dislocations and cementite in pearlitic steels at different drawing strains using X-ray diffraction, ISIJ Int. 53 (4) (2013) 673–679.
[79] A. Taniyama, T. Takayama, M. Arai, T. Hamada, Deformation behavior of cementite in deformed high carbon steel observed by X-ray diffraction with synchrotron radiation, Metall. Mater. Trans. A 48 (2017) 4821–4830.